TO THE 40TH ANNIVERSARY OF THE JOINT INSTITUTE FOR NUCLEAR RESEARCH

The quark-spin structure of the nucleon: 20 years of JINR – CERN collaboration †

R Voss

Contents

Abstract. A review is presented of the 20 years of collaboration between JINR (Dubna) and CERN in the field of deep-inelastic muon – nucleon scattering, with emphasis on the precision measurements of scaling violations and on the recent studies of the internal spin structure of the nucleon.

1. Introduction

The physics of deep-inelastic muon scattering to study the internal quark-spin structure of the proton and the neutron has been one of the pillars of the successful collaboration between JINR and CERN during the past 20 years. JINR has contributed to two major CERN's projects active in this area of particle physics: the NA4 experiment of the Bologna – CERN – Dubna – Munich – Saclay (BCDMS) collaboration, and the NA47 experiment of the Spin – Muon Collaboration (SMC). Both experiments were performed in the high-energy muon beam of CERN's Super Proton Synchrotron (SPS).

In this short article I cannot review the history of 25 years of Deep Inelastic Scattering (DIS) in detail but will focus on

† Report presented at the JINR Scientific Council Session on the occasion of the 40th anniversary of the Institute.

R Voss CH-1211 Geneva 23, Switzerland
E-mail: rudiger.voss@cern.ch

highlights from these two experiments, in particular those which are relevant for tests of Quantum Chromodynamics (QCD). I cannot discuss here the exciting early history of the field, i.e. the discovery of scaling and the development of the Quark – Parton Model (QPM), which has been the subject of excellent books and reports [1]. Also, this paper is not intended to compete with textbooks [2 – 5] and many review articles which have been produced on the subject earlier; most of them concentrate on either neutrino or muon scattering [6 – 10]. These papers should be consulted for a more comprehensive introduction. I will also not review in this paper nuclear effects and shadowing [11], and electroweak interference [12, 13, 8].

2. Deep inelastic scattering and the quark – parton model

2.1 The deep inelastic cross section
The lowest order diagram for deep-inelastic muon scattering

$$\mu + N \rightarrow \mu + X \qquad (1)$$

is shown in Fig. 1. For neutral current reactions, the interaction can be mediated by a virtual photon or Z boson. At present fixed target energies, the cross-section for scattering of charged leptons is dominated by virtual photon exchange. In this paper, I will discuss only inclusive scattering where the scattering amplitudes are summed over all possible hadronic final states. In this case, the inclusive cross-section can be written as a function of two independent kinematic
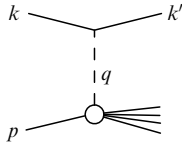
Figure 1. The lowest order Feynman diagram for deep inelastic lepton scattering.

variables. One usually chooses two of the following Lorentz invariant variables:

(a) the squared four-momentum transfer

$$Q^2 = -q^2 = -(k - k')^2 = 4EE' \sin^2 \frac{\theta}{2} ; \qquad (2)$$

(b) the energy transfer to the hadronic system

$$v = p \, \frac{q}{M} = E' - E ; \qquad (3)$$

(c) the Bjorken scaling variable

$$x = \frac{Q^2}{2p} \, q = \frac{Q^2}{2Mv} ; \qquad (4)$$

(d) and the scaling variable

$$y = \frac{(p \cdot q)}{(p \cdot k)} = \frac{v}{E} . \qquad (5)$$

In these equations, k, k', p, and q are the four-vectors of the initial and final states of lepton, the target nucleon, and the exchanged boson. M is the mass of the target nucleon, whereas the lepton mass has been neglected. E, E', and θ are the energies of the incident and scattered lepton, and the lepton scattering angle in the laboratory frame.

Neglecting lepton masses, the cross-section for unpolarised charged lepton scattering in virtual photon exchange approximation, can be written as

$$\frac{\mathrm{d}^2\sigma}{\mathrm{d}Q^2 \, \mathrm{d}x} = \frac{4\pi\alpha^2}{Q^4} \frac{1}{x} \left[xy^2 F_1(x, Q^2) \right.$$
$$\left. + \left(1 - y - \frac{Mxy}{2E}\right) F_2(x, Q^2) \right], \qquad (6)$$

where α is the electromagnetic coupling constant and $F_1(x, Q^2)$ and $F_2(x, Q^2)$ are the unpolarised structure functions of the nucleon.

2.2 Structure functions in the quark – parton model
In the so-called 'naive' QPM, the Bjorken variable x takes the simple meaning of the fraction of nucleon three-momentum that is carried by the quark struck in the interaction. This interpretation is strictly valid only in the Breit frame or infinite momentum frame, where the quark masses and transverse momenta are neglected. To a good approximation, it holds for experiments at present accelerator energies.

In the same reference frame, assuming that quarks are pointlike non-interacting particles, the structure functions depend on a single dimensionless variable only. They can be interpreted as linear combinations of 'quark distribution

functions' $q(x)$, which are probability densities of quarks in the variable x.

For charged lepton scattering †,

$$F_1(x) = \frac{1}{2} \sum_i e_i^2 \left[q_i(x) + \overline{q}_i(x) \right] , \qquad (7)$$

$$F_2(x) = x \sum_i e_i^2 \left[q_i(x) + \overline{q}_i(x) \right] , \qquad (8)$$

where the e_i are the electric charges of the quarks and the index i runs over all quark flavours.

From Eqns (7) and (8), it follows that

$$F_2(x) = 2xF_1(x) . \qquad (9)$$

This is the Callan–Gross relation [14] which is intimately related to the fact that quarks have spin 1/2. Again, this relation is strictly valid in the infinite momentum frame only. The violation of the Callan–Gross relation at finite energies is expressed by introducing the longitudinal structure function

$$F_\mathrm{L}(x) = F_2(x)\left(1 + \frac{4M^2x^2}{Q^2}\right) - 2xF_1(x) , \qquad (10)$$

which in turn is related to the ratio R of absorption cross-section for longitudinally and transversely polarised virtual photons:

$$R = \frac{\sigma_\mathrm{L}}{\sigma_\mathrm{T}} = \frac{F_\mathrm{L}}{2xF_1} . \qquad (11)$$

3. The BCDMS experiment

The deep-inelastic muon and neutrino scattering program has been one of the landmarks of experimentation at CERN's SPS. When this program took shape in the mid-Seventies, two big detectors were conceived to study muon scattering with unprecedented accuracy. The European Muon Collaboration (EMC) designed a versatile multi-purpose spectrometer system around a large aperture dipole magnet [16]; the BCDMS collaboration, under the influence of the successful SLAC experiments that led to the experimental discovery of partons, aimed mostly at measuring the scaling properties of nucleon structure functions with the highest possible accuracy.

To compensate for the relatively low intensity of the muon beam, they built a detector based on a very long (50 m) toroidal iron magnet, enclosing an almost equally long target [17] (Fig. 2).

The magnet was instrumented with scintillation trigger counters and multiwire proportional chapters to detect and measure the scattered muons. In a major logistic achievement, JINR contributed to this experiment the iron for the spectrometer magnet (1200 tons in the form of 320 carefully machined disks of 2.75 m diameter) and the construction of one half of the proportional chambers. By its design, the physics scope of this apparatus was limited to the study of inclusive muon scattering in a restricted kinematic region at

---

† The third structure function $xF_3(x)$ appears in deep-inelastic neutrino scattering.
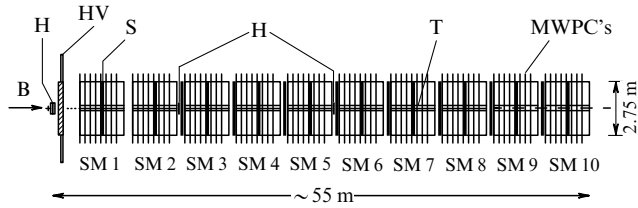
Figure 2. Schematic view of the BCDMS (NA4) apparatus: B — beam, H — hodoscopes, HV — halo-veto, S — segmented trigger counters (20 planes), T — target (8 units), MWPC's (80 planes) — multiwire proportional chambers, SM1 – SM10 — 10 identical modules.

large x. The kinematic acceptance of the apparatus was later enlarged at the expense of sacrificing a part of the luminosity. Still, the enormous length of the target allowed for a much higher statistical accuracy than could be achieved with the EMC apparatus. Best known among the BCDMS results are the high statistics measurements of the structure functions $F_2(x, Q^2)$ and $R = \sigma_L/\sigma_T$ on proton, deuterium, and carbon targets, the study of nuclear effects in deep-inelastic scattering first discovered by the EMC, and the unique measurement of weak-electromagnetic interference effects in deep inelastic muon-carbon scattering. In this review I will concentrate on the precision measurement of scaling violations in nucleon structure functions.

4. BCDMS measurements of nucleon structure functions

Together with electron scattering data from SLAC, and with results from neutrino scattering, the BCDMS data form today the backbone of our experimental understanding † of the nucleon structure function F_2 in the kinematic region of large x and Q^2. They were later complemented by results from the NMC experiment at CERN and the E665 experiment at Fermilab in a kinematic region centred at smaller x and Q^2, and recently by results from the electron – proton collider HERA at DESY, exploring a totally new kinematic domain at even smaller x but very high Q^2.

The experiment initially took data with a carbon target from 1978 until 1980; structure function results from this run were published in Ref. [18] and are shown in Fig. 3.

During the SPS shut-down of 1980 – 1981, the experiment was upgraded for enhanced detection capabilities at small scattering angles in order to enlarge the kinematic acceptance at small values of x. In this configuration, the experiment took data from 1981 until 1985 with hydrogen [19] and deuterium [20] targets; these data cover a region of large x and Q^2 ($x \geqslant 0.07$, $Q^2 > 10$ GeV^2) and have proven to be a powerful tool to test perturbative QCD and to measure the strong coupling constant (see Section 5).

As an example, the proton data are shown in Fig. 4 together with SLAC results [21], and with later data from NMC [63] and E665 [23] experiments.

† For years, this understanding has been plagued by disagreements between the EMC and BCDMS results on F_2. The NMC collaboration remeasured this structure function with the upgraded EMC spectrometer, and decided eventually in favour of BCDMS.
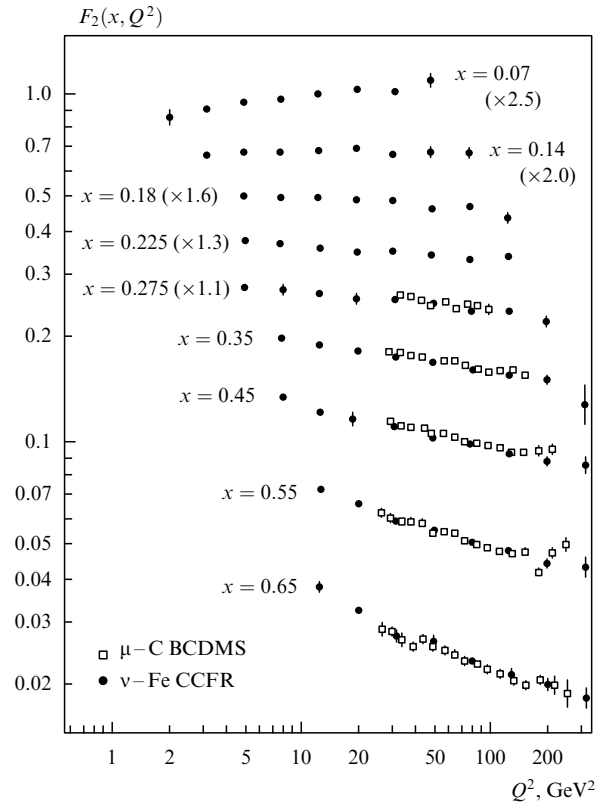

Figure 3. The nucleon structure function F_2 measured by BCDMS collaboration in deep inelastic scattering of muons on carbon. Data from neutrino scattering on iron from the CCFR collaboration at Fermilab are shown for comparison. The data are shown versus Q^2, for bins of fixed x, and have been scaled by the factors shown in parentheses.

5. Tests of quantum chromodynamics

High statistics measurements of $F_2(x, Q^2)$ and $xF_3(x, Q^2)$ and sophisticated QCD analyses have firmly established the validity of the Altarelli – Parisi equations as the correct description of scaling violations observed in deep inelastic scattering. The emphasis of QCD studies in this field has therefore gradually shifted from qualitative QCD tests to accurate determinations of the strong coupling constant α_s and the gluon distribution.

5.1 Scaling violations in perturbative QCD
A comprehensive review of perturbative QCD is beyond the scope of these lectures. Reference [24] is the classical paper on this subject; excellent introductions can be found in Refs [10, 25]. Again, the following is mainly a brief reminder of the essential formalism that is needed to analyse scaling violations of nucleon structure functions.

The Q^2 evolution of the strong coupling constant α_s is controlled by the renormalisation group equation of QCD. The 'canonical' — but by no means unique — solution usually adopted for the analysis of deep inelastic data is, in Next-to-Leading Order (NLO),

$$\alpha_s(Q^2) = \frac{4\pi}{\beta_0 \ln(Q^2/\Lambda^2)} \left[1 - \frac{\beta_1}{\beta_0^2} \frac{\ln \ln(Q^2/\Lambda^2)}{\ln(Q^2/\Lambda^2)} \right], \qquad (12)$$

where the so-called beta functions are given by

$$\beta_0 = 11 - \frac{2}{3} N_f, \qquad \beta_1 = 102 - \frac{38}{3} N_f$$
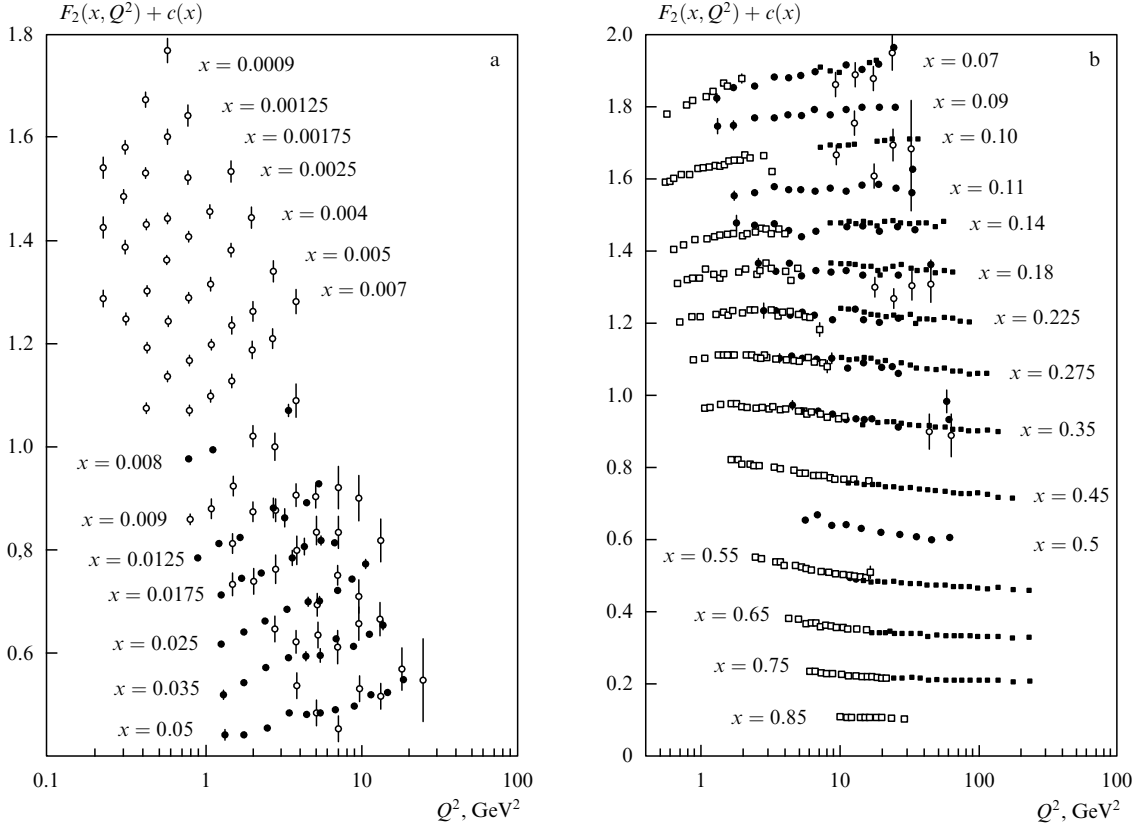
Figure 4. The proton structure function F_2^p measured in electromagnetic scattering of electrons (SLAC — □) and muons (BCDMS — ■, E665 — ○, NMC — ●), shown as a function of Q^2 for bins of fixed x. Only statistical errors are shown. For the purpose of plotting, a constant $c(x) = 0.1i_x$ is added to F_2^p where i_x is the number of the x bin, ranging from 1 ($x = 0.05$) to 14 ($x = 0.0009$) (a) and from 1 ($x = 0.85$) to 15 ($x = 0.07$) (b).

and N_f is the effective number of active quark flavours in the scattering process.

The parameter Λ is the so-called 'mass scale' of QCD and has the physical meaning of a typical energy at which the running coupling constant [Eqn (12)] becomes large and the perturbative expansion breaks down. Its value is not predicted by QCD and can only be determined by experiment. Since α_s is the physical observable, the numerical value of Λ depends on N_f and, beyond leading order, on the renormalisation scheme assumed to compute the perturbative QCD expansions. In deep inelastic scattering, $N_f = 4$ at fixed target energies and the so-called 'modified minimal subtraction' scheme ($\overline{\text{MS}}$) [26] are usually assumed, and the corresponding Λ is written $\Lambda^{(4)}_{\overline{\text{MS}}}$. When comparing measurements of α_s or Λ from processes with different N_f, care must be exercised when crossing the flavour threshold since $\alpha_s(Q^2)$ is, of course, continuous.

To introduce the QCD-improved QPM, we have to distinguish between quark distributions which are singlets and non-singlets in flavour space. Any structure function can be decomposed into a linear combination of flavour singlet (SI) and non-singlet (NS) structure functions. In NLO, these structure functions are related to 'effective' quark distributions $q^{\text{SI}}(x, Q^2)$ and $q^{\text{NS}}(x, Q^2)$ by

$$F_i^{\text{NS}}(x, Q^2) = C_i x q^{\text{NS}}(x, Q^2)$$

$$+ C_i x \frac{\alpha_s(Q^2)}{2\pi} \int_x^1 q^{\text{NS}}(t, Q^2) f_{iq}\left(\frac{x}{t}\right) \frac{dt}{t} , \quad (13)$$

$$F_i^{\text{SI}}(x, Q^2) = C_i' x q^{\text{SI}}(x, Q^2)$$

$$+ C_i' x \frac{\alpha_s(Q^2)}{2\pi} \int_x^1 q^{\text{SI}}(t, Q^2) f_{iq}\left(\frac{x}{t}\right) \frac{dt}{t}$$

$$+ C_i'' x \frac{\alpha_s(Q^2)}{2\pi} \int_x^1 G(t, Q^2) f_{iG}\left(\frac{x}{t}\right) \frac{dt}{t} , \quad (14)$$

where $G(x, Q^2)$ is the gluon distribution, C_i, C_i', and C_i'' are coefficients, and f_{iq} and f_{iG} are so-called coefficient functions. In this picture, q^{SI} and q^{NS} are 'bare' quark distributions that cannot be measured directly by experiment. In the QCD leading order QCD, the convolution terms are neglected and Eqns (13) and (14) become equivalent to, e.g., Eqn (8).

The Q^2 evolution of the effective quark and gluon distribution is predicted by the Altarelli – Parisi equations [27]†:

$$\frac{dq^{\text{NS}}(x, Q^2)}{d \ln Q^2} = \frac{\alpha_s(Q^2)}{2\pi} \int_x^1 q^{\text{NS}}(t, Q^2) P^{\text{NS}}\left(\frac{x}{t}\right) \frac{dt}{t} , \quad (15)$$

$$\frac{dq^{\text{SI}}(x, Q^2)}{d \ln Q^2} = \frac{\alpha_s(Q^2)}{2\pi} \int_x^1 \left[q^{\text{SI}}(t, Q^2) P_{qq}\left(\frac{x}{t}\right) \right.$$

$$\left. + C_q G(t, Q^2) P_{qG}\left(\frac{x}{t}\right) \right] \frac{dt}{t} , \quad (16)$$

† These equations are also known as the Altarelli–Lipatov–Parisi ones. (*Scientific adviser's note*)

$$\frac{\mathrm{d}G(x,Q^2)}{\mathrm{d}\ln Q^2} = \frac{\alpha_s(Q^2)}{2\pi}\int_x^1\left[G(t,Q^2)P_{GG}\left(\frac{x}{t}\right)\right.$$
$$\left. + C_G q^{SI}(t,Q^2)P_{Gq}\left(\frac{x}{t}\right)\right]\frac{\mathrm{d}t}{t}\,, \qquad (17)$$

where the C_i are another set of coefficients and P^{NS}, P_{qq}, etc. are so-called splitting functions describing the QCD diagrams. Both coefficient functions and splitting functions can be calculated in perturbative QCD as power series in α_s. In NLO and beyond, terms of $O(\alpha_s)$ and higher can be absorbed by either of them, an ambiguity known as 'factorisation scheme dependence', and care must be taken to use consistent splitting and coefficient functions.

5.2 Measurement of the strong coupling constant

The F_2 measurements of BCDMS collaboration at large x and Q^2 with carbon, hydrogen, and deuterium targets were the first high statistics data that yielded a conclusive determination of Λ_{QCD} [28, 29, 20]. The structure function $F_2(x,Q^2)$ is, in general, a linear combination of both flavour singlet and non-singlet quark distributions. Its Q^2 evolution is described by the Altarelli – Parisi equations (15) and (16) that also depend on the gluon distribution. The original BCDMS fits to the hydrogen and deuterium data were later superseded by a very careful analysis by Virchaux and Milsztajn of the combined SLAC and BCDMS hydrogen and deuterium data [30]. Since the SLAC data extend down to four-momentum transfers as low as $Q^2 = 1$ GeV^2, these authors make an allowance for non-perturbative 'higher twist' contributions to the observed scaling violations at small Q^2. These higher twist effects are mostly due to long-distance final state interactions which are difficult to calculate in perturbative QCD and there is little theoretical prejudice about their kinematical dependence except that they can be expanded into power series in $1/Q^2$ [31]. This suggests an ansatz

$$F_2(x,Q^2) = F_2^{LT}(x,Q^2)\left[1 + \frac{C_{HT}(x)}{Q^2}\right], \qquad (18)$$

where the leading twist structure function F_2^{LT} follows the Altarelli – Parisi equations and which gives indeed a very satisfactory fit to the data (Fig. 5). The quality of the fit is best illustrated in the representation of the 'logarithmic slopes' which shows the derivative of the structure function with respect to $\ln Q^2$ as predicted by the Altarelli – Parisi equations, averaged over the Q^2 range of each bin in x (Fig. 6). In this analysis the higher twist term $C_{HT}(x)$ of Eqn (18) is fitted by a set of constants in each bin of x. The remarkable result here is that these coefficients are compatible with zero for $x < 0.4$, i.e. perturbative QCD can describe scaling violations in this region down to Q^2 as small as 1 GeV^2. The result for Λ is

$$\Lambda_{\overline{MS}}^{(4)} = 263 \pm 42 \text{ MeV},$$

where the error combines statistical and systematic uncertainties. This corresponds to a strong coupling constant at Q^2 typical of these data of

$$\alpha_s(50 \text{ GeV}^2) = 0.180 \pm 0.008\,.$$

In the same analysis Virchaux and Milsztajn have also estimated the 'theoretical' uncertainty due to the neglect of higher order terms in the perturbative QCD expansions of the splitting and coefficient functions, which can be absorbed into a redefinition of the factorisation and renormalisation scale Q and is therefore often referred to as 'scale uncertainty'. Their final result for α_s at $Q^2 = M_Z^2$ is

$$\alpha_s(M_Z^2) = 0.113 \pm 0.003(exp.) \pm 0.004(theor.)\,.$$

This result still constitutes one of the most significant inputs to the present world average of α_s. As a byproduct, this QCD fit also provides an estimate of the gluon distribution in the nucleon [see Eqn (17)]. Since the gluon distribution is strongly peaked at small x, however, this estimate is now superseded by fits to more recent data with better coverage of this kinematic region.

6. Polarised deep inelastic lepton scattering

Since several years, deep inelastic scattering with polarised beams and targets is experiencing a Renaissance, in the wake of the seminal 1988 EMC discovery [32] that the spin-dependent structure function of the proton violated the Ellis – Jaffe sum rule [33], and that the quarks appear to carry only a small fraction of the total spin of the proton. This result has raised questions about the origin of the nucleon spin at the parton level which have not yet been answered conclusively. It has therefore triggered intense theoretical and experimental activities, which have resulted in a plethora of papers and in a new generation of experiments to study the internal spin structure of the nucleon.

I start by giving a brief overview of the basic phenomenology of cross-section asymmetries (Section 6), and concentrate on experimental techniques (Section 7), and recent experimental results (Sections 8 – 10). An introduction into the theoretical situation can be found in Refs [34, 35].

6.1 The deep inelastic cross-section

In the laboratory system the scattering process is conveniently visualised in the two planes depicted in Fig. 7. The scattering plane is defined, as in the unpolarised case, by the momentum 3-vectors $\mathbf{k}$ and $\mathbf{k}'$ of the incoming and scattered lepton, respectively; θ is the scattering angle. The spin plane is defined by $\mathbf{k}$ and the spin vector $\mathbf{S}_N$ of the nucleon; β is the angle between $\mathbf{k}$ and $\mathbf{S}_N$ ($0 \leqslant \beta \leqslant \pi$) and ϕ is the angle between the scattering and the spin planes.

The differential deep inelastic cross-section for the process shown in Fig. 7 can be decomposed into an unpolarised piece σ_0 and a polarised piece $\Delta\sigma$,

$$\frac{\mathrm{d}^3\sigma(\beta)}{\mathrm{d}x\,\mathrm{d}y\,\mathrm{d}\phi} = \frac{\mathrm{d}^3\sigma_0}{\mathrm{d}x\,\mathrm{d}y\,\mathrm{d}\phi} - \frac{\mathrm{d}^3\left[\Delta\sigma(\beta)\right]}{\mathrm{d}x\,\mathrm{d}y\,\mathrm{d}\phi}\,, \qquad (19)$$

where $\mathrm{d}^3\sigma_0/\mathrm{d}x\,\mathrm{d}y\,\mathrm{d}\phi$ is the familiar unpolarised deep inelastic cross-section depending on the spin-independent structure functions F_1 and F_2. In the Born approximation, the polarised contribution is given by Ref. [36]

$$\frac{\mathrm{d}^3\left[\Delta\sigma(\beta)\right]}{\mathrm{d}x\,\mathrm{d}y\,\mathrm{d}\phi} = \frac{4\alpha^2}{Q^2}\left\{\cos\beta\left[\left(1 - \frac{y}{2} - \frac{\gamma^2 y^2}{4}\right)g_1(x,Q^2)\right.\right.$$
$$\left.- \frac{\gamma^2 y}{4}g_2(x,Q^2)\right] - \cos\phi\sin\beta\,\frac{\sqrt{Q^2}}{\nu}$$
$$\left.\times\left(1 - y - \frac{\gamma^2 y^2}{4}\right)^{1/2}\left[\frac{y}{2}g_1(x,Q^2) + g_2(x,Q^2)\right]\right\}, \quad (20)$$

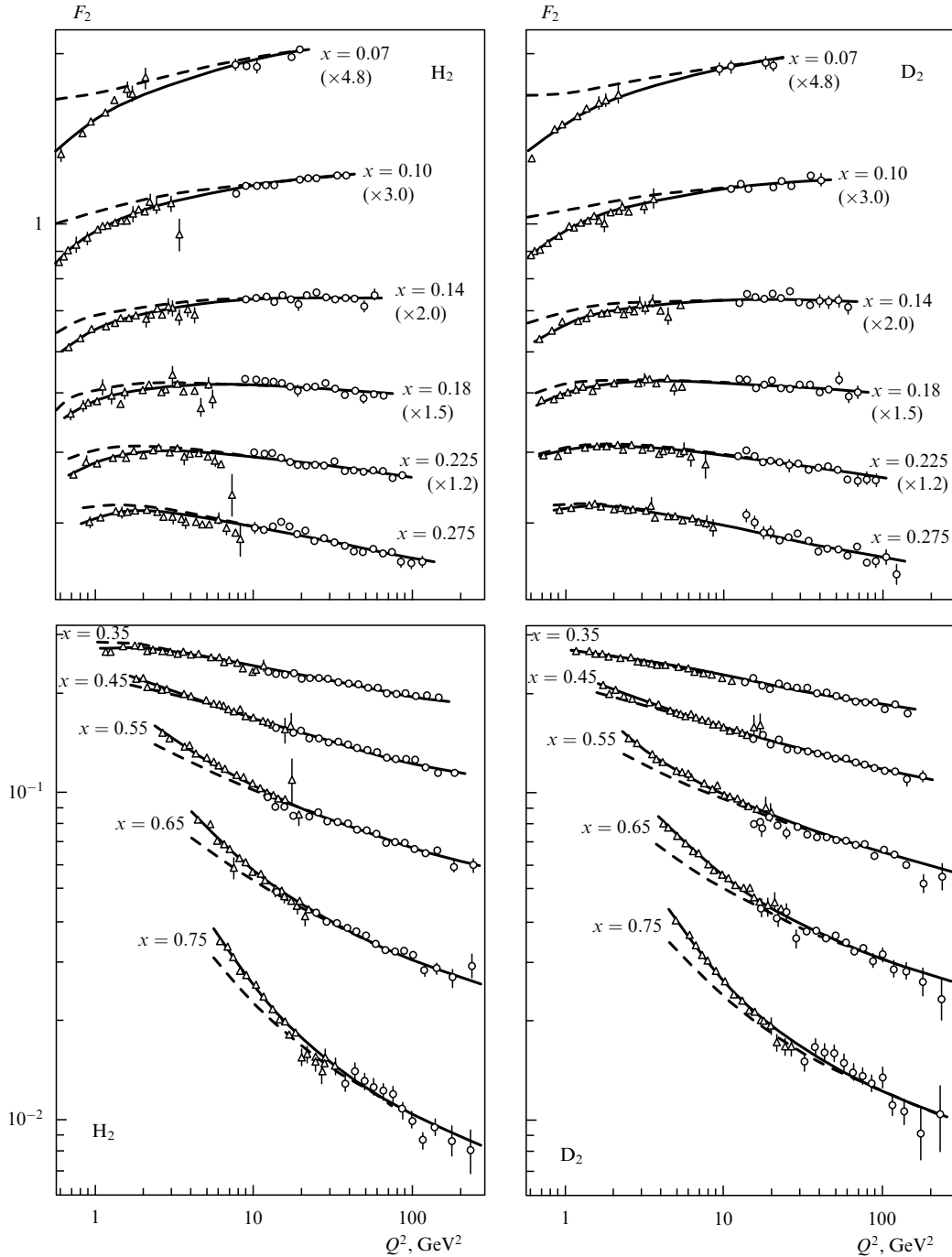**Figure 5.** The QCD fit to the SLAC ($\triangle$) and BCDMS ($\circ$) data on $F_2(x, Q^2)$. The dashed line is the purely perturbative fit with the leading twist structure function $F_2^{\mathrm{LT}}(x, Q^2)$. The solid line includes the higher twist contribution discussed in the text.

where

$$\gamma = \frac{2Mx}{\sqrt{Q^2}}, \tag{21}$$

and g_1, g_2 are the spin-dependent structure functions of the nucleon. In these expressions, M is the nucleon mass, Q^2 is the four-momentum transfer to the target nucleon, and x and y are the familiar scaling variables.

An inspection of Eqn (20) reveals immediately how the two structure functions g_1 and g_2 can be disentangled from measurements of the differential cross-section. A target

polarisation parallel to the beam direction, i.e. $\sin \beta = 0$, mainly projects out g_1 since the contribution from g_2 is suppressed at high energies by the factor $Mx/2E$. For $\cos \beta = 0$, i.e. transverse target polarisation, g_1 and g_2 contribute to the cross-section with similar weights.

6.2 Cross section asymmetries
The polarised piece (20) gives only a small contribution to the cross-section and is, in general, experimentally further suppressed by incomplete beam and target polarisations. It is therefore customary to evaluate it from measurements of cross-section asymmetries in which the unpolarised part in
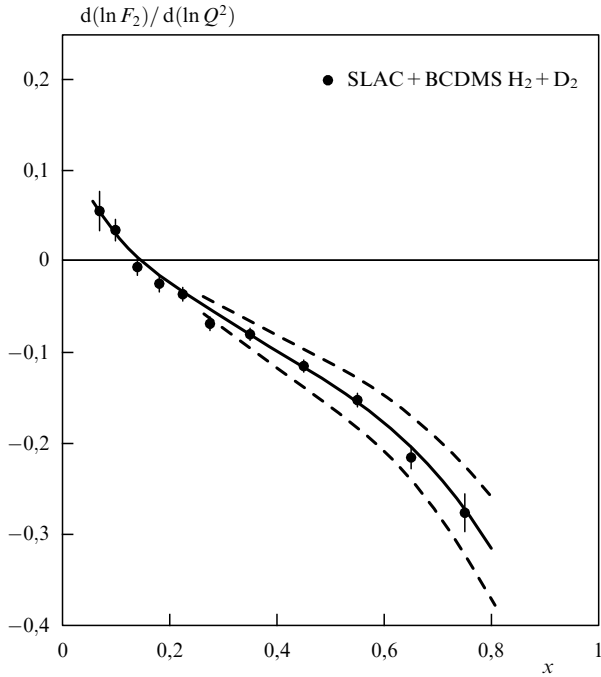
Figure 6. Scaling violations $\mathrm{d}(\ln F_2)/\mathrm{d}(\ln Q^2)$ observed in the combined SLAC/BCDMS hydrogen and deuterium data. Errors are statistical only. The solid line is a QCD fit corresponding to $\alpha_s(M_Z^2) = 0.113$; the dashed lines correspond to $\Delta\alpha_s(M_Z^2) = 0.010$.
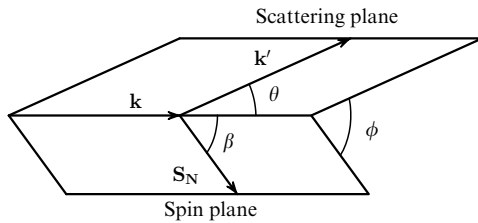

Figure 7. Scattering of longitudinally polarised leptons in the laboratory frame.

Eqn (19) cancels. When both the beam and the target are longitudinally polarised ($\sin\beta = 0$), this asymmetry is

$$A = \frac{\sigma^{\uparrow\downarrow} - \sigma^{\uparrow\uparrow}}{\sigma^{\uparrow\downarrow} + \sigma^{\uparrow\uparrow}} \, , \tag{22}$$

where $\sigma^{\uparrow\downarrow}$ and $\sigma^{\uparrow\uparrow}$ are the cross-sections for opposite and equal spin directions, respectively. For simplicity, terms of order γ^2 are neglected in the following discussion. From Eqn (20), one finds

$$A = D[A_1 + \eta A_2] \, , \tag{23}$$

where

$$A_1(x) = \frac{g_1(x)}{F_1(x)} \, , \tag{24}$$

$$A_2(x) = \gamma \, \frac{g_1(x) + g_2(x)}{F_1(x)} \, ; \tag{25}$$

D is often called the depolarisation factor of the virtual photon and is given by

$$D = \frac{2y - y^2}{2(1 - y)(1 + R) + y^2} \, ; \tag{26}$$

the factor η depends only on kinematic variables:

$$\eta = \frac{\sqrt{Q^2}}{E} \, \frac{2(1 - y)}{y(2 - y)} \, . \tag{27}$$

A_1 and A_2 can be interpreted as virtual photon – nucleon asymmetries. For spin-$(1/2)$ targets (proton and neutron),

$$A_1^{\mathrm{p,n}} = \frac{\sigma_{1/2} - \sigma_{3/2}}{\sigma_{1/2} + \sigma_{3/2}} \, , \tag{28}$$

$$A_2^{\mathrm{p,n}} = \frac{2\sigma^{\mathrm{TL}}}{\sigma_{1/2} + \sigma_{3/2}} \, , \tag{29}$$

whereas for the deuteron [37]

$$A_1^{\mathrm{d}} = \frac{\sigma_0 - \sigma_2}{\sigma_0 + \sigma_2} \, , \tag{30}$$

$$A_1^{\mathrm{d}} = \frac{\sigma_0^{\mathrm{TL}} + \sigma_1^{\mathrm{TL}}}{\sigma_0 + \sigma_2} \, . \tag{31}$$

In these expressions the indices refer to the total spin projections of the photon – hadron system in the direction of the virtual photon, and the σ^{TL} are cross-sections arising from the interference of amplitudes for longitudinally and transversely polarised virtual photons. The following bounds can be derived for A_1 and A_2 [38]:

$$|A_1| \leqslant 1 \, , \qquad |A_2| \leqslant R \, ; \tag{32}$$

for this reason, A_2 is expected to give a small contribution to A.

Finally, the experimentally measured counting rate asymmetry is related to the cross-section asymmetry (22) by

$$A_{\mathrm{exp}} = f_{\mathrm{t}} P_{\mathrm{t}} P_{\mathrm{b}} A \, , \tag{33}$$

where P_{b} is the beam polarisation, P_{t} is the polarisation of the target nucleons, and f_{t} is the target dilution factor, i.e. the fraction of polarised nucleons in the target material.

6.3 Spin-dependent structure functions in the quark – parton model

Similar to the spin-independent structure functions, the spin-dependent structure function g_1 also has a straightforward interpretation in the QPM:

$$g_1(x) = \frac{1}{2} \sum_i e_i^2 [q_i^+(x) - q_i^-(x)] \, , \tag{34}$$

where $q_i^+(x)$ [$q_i^-(x)$] is the density of quarks with helicity parallel (antiparallel) to the nucleon spin. This interpretation of $g_1(x)$ can be understood from the fact that a virtual photon with spin projection $+1$ can only be absorbed by a quark with spin projection $-1/2$, and vice versa.

The interpretation of the 'transverse' spin structure function g_2 in the QPM is less obvious and has been the subject of theoretical debate [36, 39]. Wandzura and Wilczek

[40] have shown that in QCD it can be decomposed as

$$g_2(x, Q^2) = g_2^{WW}(x, Q^2) + \overline{g}_2(x, Q^2), \qquad (35)$$

where the 'trivial' piece g_2^{WW} is a leading twist contribution in the jargon of QCD, and is completely determined by $g_1(x, Q^2)$:

$$g_2^{WW}(x, Q^2) = -g_1(x, Q^2) + \int_x^1 g_1(y, Q^2) \frac{dy}{y}. \qquad (36)$$

The term $\overline{g}_2(x, Q^2)$ is a twist-3 contribution which is best understood in an Operator Product Expansion (OPE) analysis in QCD, where it is sensitive to a quark–gluon correlation function in the nucleon and thus contains unique new physics.

7. The SMC experiment

In the new generation of experiments that has been set up following the 1988 EMC discovery, three set-ups using different experimental techniques can be distinguished (Table 1):

(1) The experiment of SMC at CERN, using a high-energy muon beam and cryogenic solid state targets [42];

(2) Experiments E142, E143, E154 and E155 at SLAC, using electron beams, a liquid ^{3}He target, and also cryogenic solid state targets [43];

(3) The HERMES experiment at DESY, using the polarised electron beam of the electron–proton storage ring HERA and internal hydrogen, deuterium, and ^{3}He gas targets [44].

Table 1. New experiments on polarised deep-inelastic lepton–nucleon scattering. The last column shows references to the principal physics results obtained until now.

Experiment	Beam	Year	Beam energy, GeV	Target	Ref.
SMC	μ^+	1992	100	C_4D_9OD	[50]
		1993	190	C_4H_9OH	[51, 52]
		1994	190	C_4D_9OD	[53]
		1995	190	C_4D_9OD	
		1996	190	NH_3	
E142	e^-	1992	19.4–25.5	^{3}He	[55]
E143	e^-	1993	29.1	NH_3, ND_3	[56, 57]
E155	e^-	1995	50	^{3}He	
	e^-	1996	50	NH_3, ND_3	
HERMES	e^+	1995	27.5–35	H, D, ^{3}He	

Electron and muon beam experiments are complementary in their physics reach. The main advantage of SLAC and HERMES experiments is the enormous beam intensity that is available from electron accelerators. The strength of the SMC experiment is the higher beam energy, which ensures a better kinematic coverage both at large Q^2 and in the region of small Bjorken x critical for sum rule tests (Fig. 8). However, the muon intensity is limited due to the small net event yield from the decay chain p $\rightarrow \pi(K) \rightarrow \mu$ which is employed to produce muon beams at high-energy proton accelerators. The systematic errors of all experiments are presently of similar size. In a nutshell, fixed-target electron beam experiments produce more precise data but are confined to a more limited kinematic range.
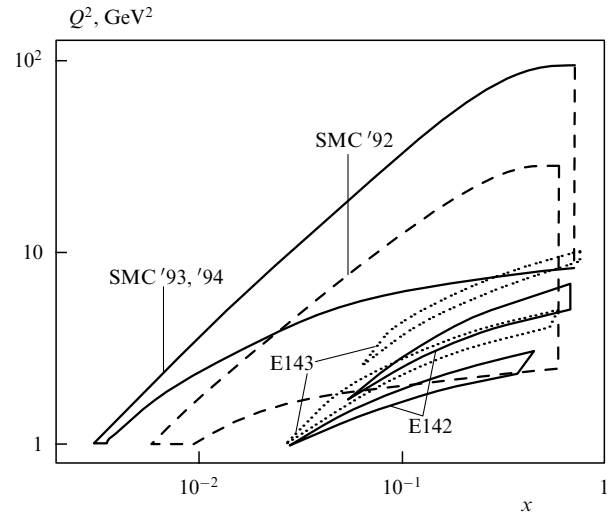

Figure 8. Kinematic ranges of recent polarised deep inelastic scattering experiments. For SMC, there are two different regions due to different beam energies used in 1992 (100 GeV) and 1993–1994 (190 GeV). For each of the two SLAC experiments E142 and E143, the two bands correspond to the two spectrometer arms.

In order to compensate partly for the modest beam intensity, the SMC solid state target is by far the largest polarised target ever built. The target materials used so far are normal and deuterated butanol. The dilution factor, i.e. the fraction of polarisable nucleons in the target molecules, is $f_p = 0.13$ and $f_d = 0.23$, respectively †. The target is subdivided into two parts of approximately 60 cm length each. They can be longitudinally polarised in opposite directions, to allow for simultaneous data taking with the two relative orientations of beam and target polarisations required to measure the asymmetry A [Eqn (22)]. The target material is placed inside a 2.5 T superconducting solenoid of high field homogeneity and cooled to temperatures of less than 50 mK with a ^{3}He–^{4}He dilution refrigerator. It is polarised using the technique of Dynamic Nuclear Polarisation (DNP); opposite polarisations in the two target halves are achieved by irradiating the material with microwaves of slightly different frequencies close to the respective electron-spin resonance frequencies. In 1992, the SMC discovered that the polarisations can be boosted substantially by suitable frequency modulation of the microwaves [45], a technique particularly beneficial to the performance of the deuteron target. Typical polarisations obtained are 50% for the deuteron and 85% for the proton target. To reduce systematic errors to a minimum, the spin directions of both target halves are reversed every few hours by rotation of the magnetic field, with minimal loss of polarisation. The field rotation is achieved by suitable dynamic superposition of a dipole field and the solenoid field.

The muon beam of CERN's SPS has a 'natural' longitudinal polarisation thanks to parity violation. In the decay $\pi(K) \rightarrow \mu\nu_\mu$, the muon and the neutrino are fully polarised in the centre-of-mass system, giving negative (positive) helicity to the positive (negative) muon. A Lorentz boost affects the

---

† The term 'dilution factor' also frequently refers to the event yield from polarised protons and deuterons, which differs from the 'naive' (chemical) dilution factor by nuclear effects and radiative corrections to the Born cross-section, and is thus a function of the kinematic variables.

longitudinal polarisation of the massive muons which in the laboratory system depends on the ratio of muon and hadron energies. SMC operates with a typical ratio of $E_\mu/E_\pi \approx 0.9$, which gives a beam polarisation of $P_b \approx -80\%$ for a μ^+ beam. The typical beam intensity is 4.5×10^7 per spill of 2.4 s duration, with a period of 14.4 s. The beam momentum is measured with a magnetic spectrometer (BMS) installed upstream of the target.

The beam polarisation is determined in a dedicated polarimeter installed downstream of the main spectrometer discussed below. For all data published to date, the beam polarisation was determined from the Michel spectrum of positrons from the decay $\mu^+ \rightarrow e^+ \nu_e \bar{\nu}_\mu$ [46]. A complementary method which employs the cross-section asymmetry of Möller scattering of muons on polarised electrons in a magnetised foil was implemented at a later stage, and will be used, in addition to the decay method, in the analysis of more recent data.

For the identification and momentum analysis of the scattered muon, the SMC uses an upgraded version of the large-acceptance magnetic spectrometer first built by the EMC [47] (Fig. 9). A high precision measurement of the scattering angle and the momentum of charged particles is provided by a large aperture dipole magnet ($\int B\,dl = 2.3$ T m) instrumented with Multiwire Proportional Chambers (MWPCs) and drift chambers. The momentum measurement stage is followed by a muon identification stage which consists of a hadron absorber and a large-surface array of streamer tubes and drift tubes †. Drift chambers and streamer tubes are complemented by MWPCs to improve the rate capability of the spectrometer close to the beam. Three arrays of scintillator hodoscopes behind the hadron absorber provide the muon trigger of the experiment.
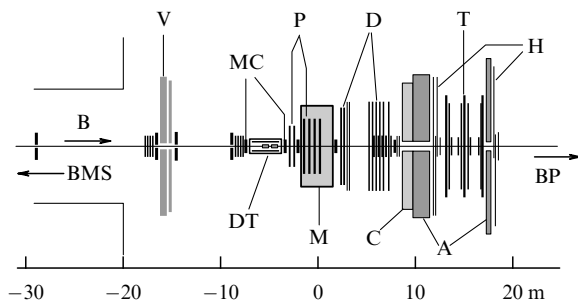
Figure 9. Side view of the SMC spectrometer: BMS — beam momentum spectrometer, B — μ-beam, V — veto counters, MC — microstrip gas chambers, P — proportional chambers, D — drift chambers, T — drift and streamer tubes, H — trigger hodoscopes, DT — polarised target, M — magnet, C — calorimeter, A — absorber, BP — beam polarimeter.

8. Results on asymmetries and spin-dependent structure functions

Results on the asymmetry A_1 and on the spin-dependent structure function g_1 have been published by E143 [56 – 58] and by SMC [50, 51, 53, 54]. Neutron results have been

† The system of drift tubes is the JINR contribution to SMS. (*Scientific adviser's note*)

published by E142 [55] and SMC has also evaluated g_1^n from the difference of proton and deuteron data [50, 53].

All present data are in excellent mutual agreement between the different experiments. As an example, a comparison of $g_1^p/F_1^p \simeq A_1^p$ [Eqn (24)] is shown in Fig. 10 [56]; similar agreement is observed for the deuteron [53]. In this figure, all data are shown at their respective average Q^2 which is about five times higher for SMC than for E143. The good agreement thus supports a key hypothesis made in the analysis of all data so far, namely that A_1 is independent of Q^2.
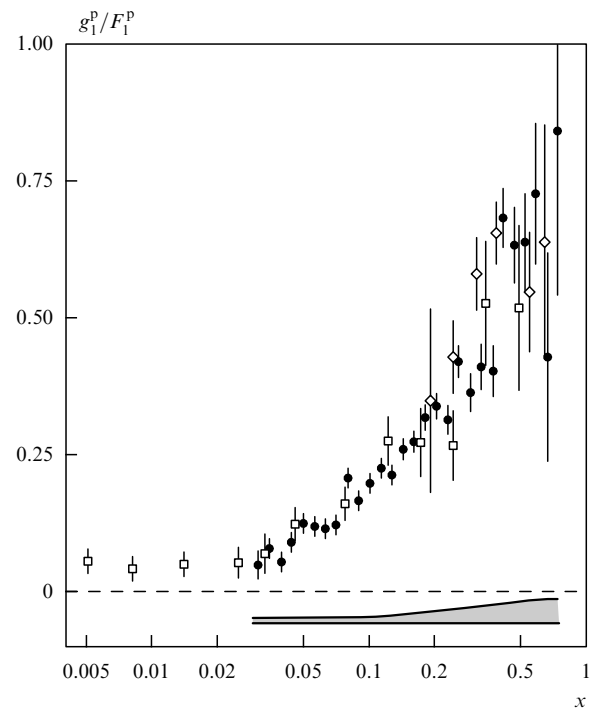
Figure 10. The ratio $g_1^p/F_1^p \simeq A_1^p$ measured by E143 ($\bullet$), SMC ($\square$) and by the earlier SLAC E130 ($\diamond$) experiment [66]. All data points are shown at the respective average Q^2, increasing from 1 GeV^2 for the small-x data to about 50 GeV^2 for the high-x SMC data. Only statistical errors are shown with the data points; the shaded band indicates the systematic errors of the E143 data.

Unfortunately, this assumption is at variance with QCD which predicts a Q^2 evolution of g_1 different from that of F_1, and thus a net Q^2 dependence of A_1. The Q^2 evolution of g_1 depends on the polarised quark and gluon densities, and no meaningful numerical predictions are possible as long as little is known about the latter. Extreme models for the polarised gluon distribution with $\Delta G(x) \approx 5$ had been studied initially [59], inspired by the anomalous gluon contribution to g_1 put forward as an explanation of the proton spin deficit [60]. Recently, Ball, Forte and Ridolfi have undertaken a detailed QCD analysis of $g_1^p(x, Q^2)$ [61]. They find that the present data poorly constrain the gluon distribution but favour a smaller ΔG.

Gehrmann and Stirling, in an analysis aimed mainly at a determination of spin-dependent parton distributions, come to similar conclusions [62].

In view of this uncertainty, the experimental groups have so far not integrated QCD technology into the analysis of their published results on g_1. Under the simple assumption that A_1 scales, the conversion of A_1 to g_1 [Eqn (24)] requires

only a parametrisation of the unpolarised structure function

$$F_1(x, Q^2) = \frac{F_2(x, Q^2)}{2x\left[1 + R(x, Q^2)\right]} \; ; \qquad (37)$$

the Q^2 dependence of g_1 is then mostly determined by the Q^2 evolution of F_2. At present, all experiments use the NMC parametrisation of F_2 [63] and the SLAC parametrisation of R [64]. The kinematic range in which these fits are valid does not cover fully the SMC data at small x; future analyses will therefore make use of recent measurements of F_2 from HERA experiments, and from Fermilab muon scattering experiment E665. The parametrisation of R is less critical since it largely cancels in the evaluation of g_1 from the experimental asymmetry [cf. Eqns (23), (24), (26), and (37)].

The recent measurement of $g_1^p(x)$ by the SMC [51] has pioneered new kinematic territory at small x and shows an indication of a rise at $x < 0.01$ (Fig. 11). The effect is on the verge of being significant, and has triggered ample theoretical speculation that will be discussed in Section 9.
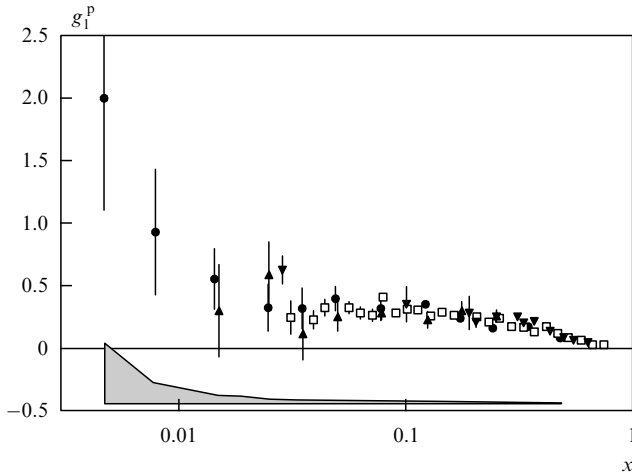

Figure 11. The spin-dependent structure function $g_1^p(x)$ of the proton at $Q^2 = 5\,\mathrm{GeV}^2$. The EMC (▲) data were re-evaluated using the same F_2 and R parametrisations as for the SMC (●) and E143 (□) data; E80/E130 (▼). Only statistical errors are shown with the data points. The SMC systematic error is indicated by the shaded areas.

All presently available deuteron and neutron data on $g_1(x)$ are compared in Fig. 12. The SMC and E143 results for the neutron are obtained from the relation $g_1^n(x) = 2g_1^d(x)/(1 - 1.5\omega_D) - g_1^p(x)$, where $\omega_D = 0.05 \pm 0.01$ [65] is the D-wave state probability of the deuteron. The SMC data clearly show that, unlike the proton data, both structure functions become negative at small x. This is in contrast to the unpolarised case where proton and neutron structure functions are very similar in this x range.

SMC has also made the first measurement of the 'transverse' asymmetry A_2^p [Eqn (25)] and of $g_2^p(x)$ with a transversely polarised proton target and a 100 GeV beam [52] (Fig. 13). A_2^p is found to be significantly below the positivity limit $|A_2| < \sqrt{R}$ and is compatible with zero, thus justifying the neglect of A_2 in the evaluation of A_1 [Eqn (23)]. Preliminary results by E143 on A_2 for the proton and the deuteron confirm this result with substantially smaller errors [67].
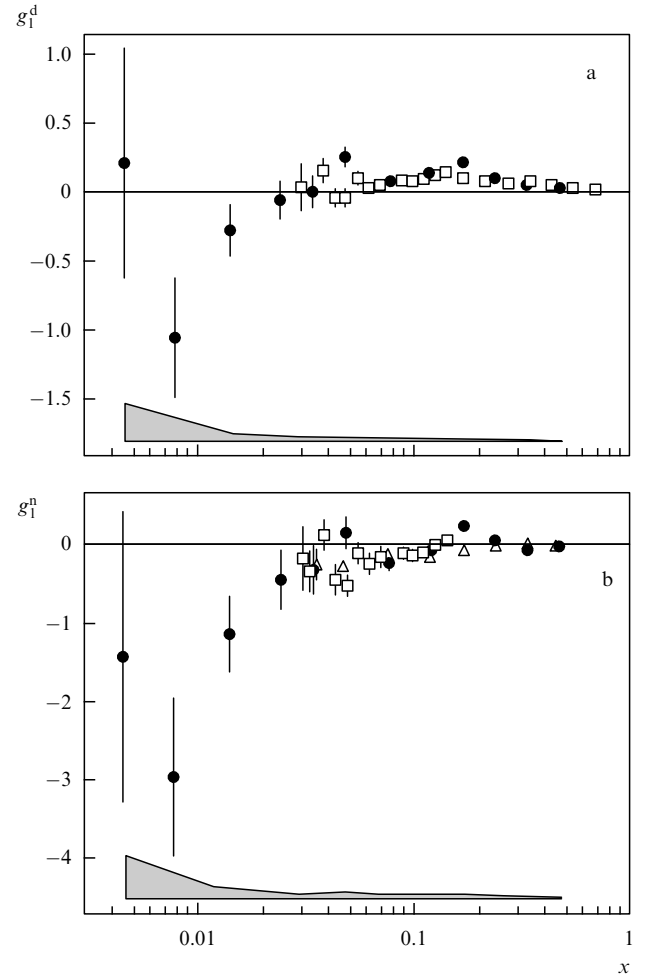

Figure 12. The spin-dependent structure functions $g_1^d(x)$ for deuteron (a) and $g_1^n(x)$ for neutron (b) at $Q^2 = 5\,\mathrm{GeV}^2$, from the SLAC E142 (△), E143 (□) and from the SMC (●). Only statistical errors are shown with the data points. The SMC systematic error is indicated by the shaded areas.
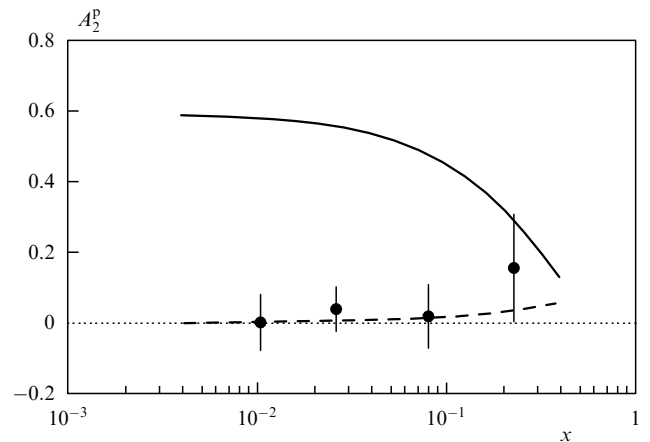

Figure 13. The asymmetry A_2^p measured by the SMC at the average Q^2 of each x bin. Only statistical errors are shown. The solid line represents the positivity limit discussed in the text, using the SLAC parametrisation of $R = \sigma_L/\sigma_T$. The dashed line is a prediction obtained from Eqns (35) and (36) for $\overline{g}_2(x) = 0$.

9. Moments of spin-dependent structure functions and sum-rule tests

9.1 Evaluating the first moment of $g_1(x)$

Sum rule tests are at the heart of testing predictions for spin-dependent structure functions. Two essential steps are involved in going from structure functions to first moments

$$\Gamma_1(Q^2) = \int_0^1 g_1(x, Q^2)\, dx;\qquad (38)$$

these are (a) evolution to a constant Q^2, and (b) extrapolation to $x = 0$ and $x = 1$. Evolving the data to a constant Q^2 invariably requires extrapolation outside the experimentally accessible range (see Fig. 8). The SLAC experiments choose a Q^2 of $2-3$ GeV^2 and the SMC uses $Q^2 = 10$ GeV^2, close to the average Q^2 of the respective data. For combined analyses, $Q^2 = 5$ GeV^2 is a reasonable choice. Again, these extrapolations are made under the hypothesis that A_1 is Q^2-independent and that the Q^2 evolution is mostly driven by F_2.

The extrapolation to $x = 1$ is not critical, since it gives a small contribution and is safely constrained by the trivial bound $A_1 < 1$. In contrast, the small-x extrapolation is the subject of debates and a source of substantial uncertainty.

The SMC and E143 assume for this a functional form $g_1(x) \propto x^\alpha$ predicted by Regge theory, α being bound by $0 \leqslant \alpha \leqslant 0.5$ [68]. Even if physically justified, there is some arbitrariness in using this form since Regge theory does not predict up to which x it is actually valid. SMC assumes $\alpha = 0$ (i.e. $g_1 =$ const) and fits this simple model to the first two data points ($x \leqslant 0.01$); the E143 does the same for $x \leqslant 0.1$. The E142 extrapolation assumes a Regge behaviour of A_1^n rather than g_1^n, $A_1^n \propto x^{\alpha'}$ with $\alpha' = 1.2$ [69].

The indication of a rise of g_1^p at small x (see Fig. 11) has given new momentum to the discussion about its different small-x behaviour. Bass and Landshoff [70] compute a contribution to the flavour singlet part of g_1^p from the exchange of two non-perturbative gluons that varies as $2\ln(1/x) - 1$. Note that such contributions do not affect tests of the Bjorken sum rule which is a pure flavour non-singlet expression. Close and Roberts [71] criticise the procedure adopted by the experiments as 'Regge Folklore' and reexamine diffraction models for the small-x behaviour. They find that rises as steep as $g_1^p \propto 1/x \log^2 x$ are allowed

and consistent with the data; such parametrisations would indeed saturate the Ellis – Jaffe sum rule. However, the same authors also point out that a dominant diffraction contribution should lead to a positive g_1 of the deuteron at small x, a conjecture not supported by the recent SMC data (Fig. 12).

Finally, perturbative QCD also predicts $|g_1(x, Q^2)|$ to rise faster than any power of $\ln 1/x$ at small x [62, 72]. The sign of g_1 is, however, not predicted by theory and depends once more on the gluon distribution.

It is important to realise that the present experiments, when estimating systematic uncertainties, make a reasonable allowance for variations of their extrapolation within the Regge model but do not account for models which predict a steeper increase (or decrease) at small x. Similarly, no Q^2 evolution of A_1 is accounted for; as was correctly pointed out in Ref. [61], the assumption that A_1 is Q^2 independent can also lead to a substantial underestimate of the errors on Γ_1. All comparisons of 'measured' moments to theoretical predictions should be looked at under these two important provisos.

9.2 Testing the Ellis – Jaffe sum rules

After this word of caution, we can compare experimental moments to the Ellis – Jaffe sum rules [33]

$$\Gamma_1^{p(n)} = +(-)\frac{1}{12}(F+D) + \frac{5}{36}(3F - D),\qquad (39)$$

where F and D are the symmetric and antisymmetric weak SU(3)$_f$ couplings, respectively, of the baryon octet.

In Table 2 and Fig. 14, a consistent set of predictions is computed from Eqn (39), using $F + D = |g_A/g_V| = 1.2573 \pm 0.0028$ [73] and $F/D = 0.575 \pm 0.016$ [74]; here, g_A and g_V are the axial and vector weak coupling constants of neutron beta decay. QCD corrections are applied following Refs [75, 76], assuming $\alpha_s(m_Z^2) = 0.117 \pm 0.005$ [73] and three quark flavours. The predictions for the EMC and SMC results at $Q^2 \simeq 10$ GeV^2 are close to the charm threshold and the 'theoretical' error therefore accounts for the effect of using four instead of three flavours. The same assumptions were made to compute the predictions for tests of the Bjorken sum rule discussed in Section 9.3.

A uniform pattern of disagreement is observed for both proton and deuteron data. The situation is less clear for the neutron where the SLAC data are very close to the Ellis – Jaffe prediction. It is tempting to relate this observation to Fig. 12

Table 2. Tests of the Ellis – Jaffe sum rules. The errors on the predictions are mostly due to the uncertainty on the strong coupling constant and F/D. In the experimental results, the first error is statistical and the second one is systematic. The EMC result also includes the earlier SLAC E80 and E130 data and is re-evaluated from Ref. [32] using up-to-date parametrisations of F_2 and R. The SMC and E143 neutron results are obtained by combining proton and deuteron data. 'Combined' refers to the combined fits discussed in the text.

| Experiment	Moment	Q^2, GeV^2	Measurement	Prediction	Ref.
EMC	Γ_1^p	10.7	$0.138 \pm 0.010 \pm 0.018$	0.170 ± 0.005	[32]
SMC	Γ_1^p	10	$0.136 \pm 0.011 \pm 0.011$	0.170 ± 0.005	[51]
	Γ_1^d	10	$0.034 \pm 0.009 \pm 0.006$	0.071 ± 0.004	[53]
	Γ_1^n	10	$-0.063 \pm 0.024 \pm 0.013$	-0.017 ± 0.004	[53]
E142	Γ_1^n	2	$-0.022 \pm 0.007 \pm 0.009$	-0.011 ± 0.006	[55]
E143	Γ_1^p	3	$0.127 \pm 0.004 \pm 0.010$	0.164 ± 0.006	[56]
	Γ_1^d	3	$0.042 \pm 0.003 \pm 0.004$	0.070 ± 0.004	[57]
	Γ_1^n	3	$-0.037 \pm 0.008 \pm 0.011$	-0.013 ± 0.005	[57]
Combined	Γ_1^p	5	0.125 ± 0.009	0.167 ± 0.005	
	Γ_1^d	5	0.041 ± 0.005	0.070 ± 0.004	
	Γ_1^n	5	-0.037 ± 0.008	-0.015 ± 0.005	
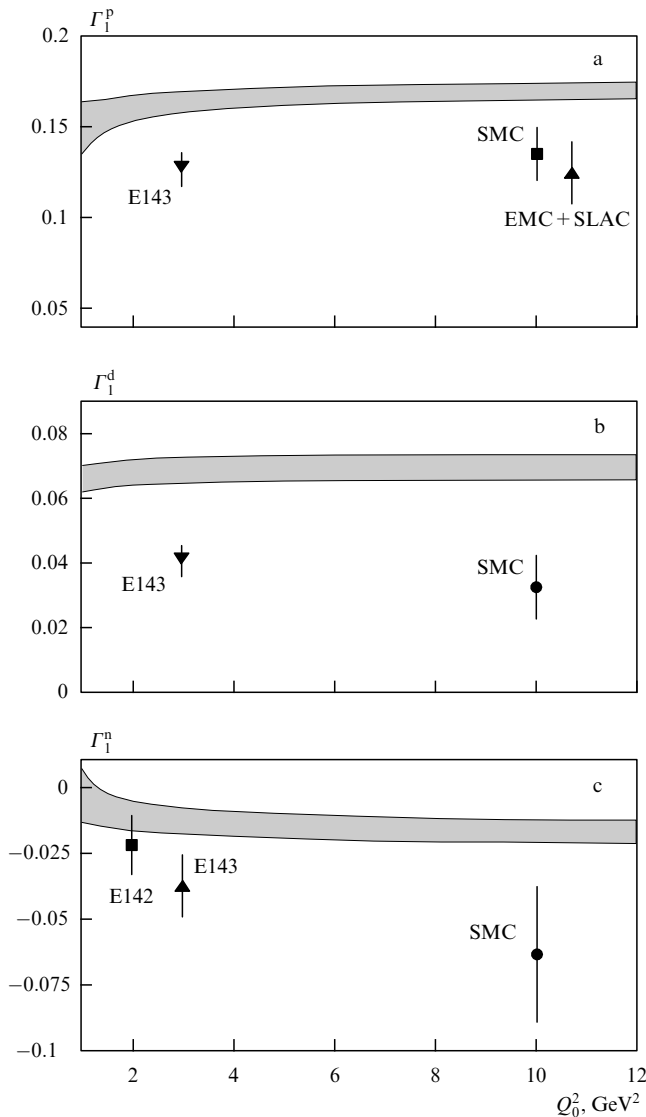
Figure 14. Tests of the Ellis – Jaffe sum rules. The predictions are shown by the shaded bands for: (a) proton, (b) deuteron and (c) neutron (see also the caption of Table 2).

which indicates that a straightforward extrapolation of the SLAC data to $x = 0$ using the Regge procedure may miss a significant negative contribution to the first moment.

For the combined result of Table 2, proton, neutron and deuteron data were first evolved to a common $Q^2 = 5 \text{ GeV}^2$. The results are obtained from a combined fit to all data given in this table which is constrained by the relation

$$\Gamma_1^{\mathrm{d}} = \frac{1}{2}\left(1 - \frac{3}{2}\,\omega_{\mathrm{D}}\right)(\Gamma_1^{\mathrm{p}} + \Gamma_1^{\mathrm{n}}).$$

The computation of errors on the combined results is not straightforward because many systematic errors, such as those on beam polarisations, are correlated between different measurements. Some uncertainties of phenomenological origin, in particular those on the F_2 parametrisation, are even correlated among results from different experimental set-ups. In the combined results shown in Table 2, all known correlations are accounted for by a Monte Carlo method.

9.3 Testing the Bjorken sum rule
The Bjorken sum rule [78 – 80]

$$\Gamma_1^{\mathrm{p}}(Q^2) - \Gamma_1^{\mathrm{n}}(Q^2) = \frac{1}{6}\left|\frac{g_{\mathrm{A}}}{g_{\mathrm{V}}}\right|\left[1 - \frac{\alpha_{\mathrm{s}}(Q^2)}{\pi} - \dots\right] \tag{40}$$

is commonly believed to be one of the most solid cornerstones of the QPM. It has escaped experimental verification for more than 25 years, notwithstanding an early claim based on proton data only [66]. It was only two years ago that serious tests became possible with the advent of precise deuteron and neutron data, in addition to the earlier proton data from SLAC and EMC. After some initial confusion [81], the consensus is now that — contrary to the Ellis – Jaffe sum rules — the Bjorken sum rule is confirmed by the data at the 10% level.

Experimentally, the most reliable results are likely to be those obtained from proton and deuteron targets, with otherwise identical experimental set-ups. E143 finds [57]

$$\Gamma_1^{\mathrm{p}} - \Gamma_1^{\mathrm{n}} = 0.163 \pm 0.010(\text{stat.}) \pm 0.016(\text{syst.})$$

at $Q^2 = 3 \text{ GeV}^2$, to be compared to a predicted

$$\Gamma_1^{\mathrm{p}} - \Gamma_1^{\mathrm{n}} = 0.177 \pm 0.005$$

at the same Q^2. The most recent SMC result is [53]

$$\Gamma_1^{\mathrm{p}} - \Gamma_1^{\mathrm{n}} = 0.199 \pm 0.038$$

at $Q^2 = 10 \text{ GeV}^2$, where the prediction is

$$\Gamma_1^{\mathrm{p}} - \Gamma_1^{\mathrm{n}} = 0.187 \pm 0.003\,.$$

The status of all presently available data is illustrated in Fig. 15 where the combined results for $Q^2 = 5 \text{ GeV}^2$ (see Table 2) are compared in the $\Gamma_1^{\mathrm{p}} - \Gamma_1^{\mathrm{n}}$ plane. The corresponding numerical result from the constrained fit discussed above is

$$\Gamma_1^{\mathrm{p}} - \Gamma_1^{\mathrm{n}} = 0.162 \pm 0.014 \quad (Q^2 = 5 \text{ GeV}^2)$$

to be compared to a predicted $\Gamma_1^{\mathrm{p}} - \Gamma_1^{\mathrm{n}} = 0.182 \pm 0.005$.
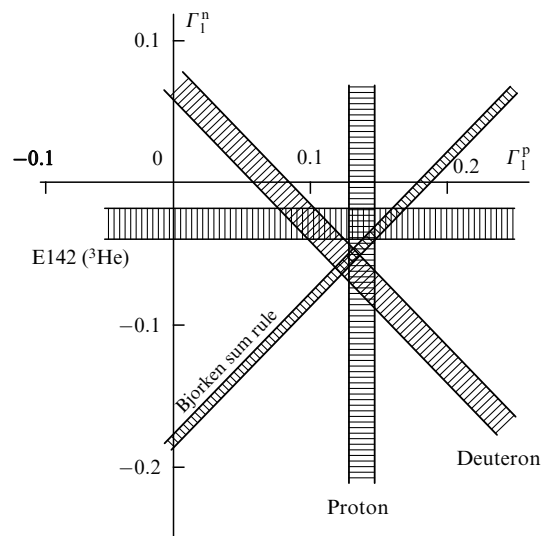
Figure 15. Experimental results and Bjorken prediction for the first moments Γ_1^{p} and Γ_1^{n} at $Q^2 = 5 \text{ GeV}^2$.

The results of the combined fit in Table 2, in particular that for Γ_1^n, as well as the above result for $\Gamma_1^p - \Gamma_1^n$ should be taken with some caution in view of the marginal consistency of the neutron data. The mutual agreement of the results for Γ_1^n is substantially improved when the small-x extrapolation of the E142 data is replaced by a fit to the muon data for g_1^n, for $x < 0.03$ (see Fig. 12). Such a fit gives $\Gamma_1^n = -0.067 \pm 0.016$ and

$$\Gamma_1^p - \Gamma_1^n = 0.203 \pm 0.023 \quad (Q^2 = 5 \text{ GeV}^2)$$

in better agreement with the prediction. In view of the large size of the QCD corrections to the Bjorken sum rule at small Q^2, one may assume its validity and exploit Eqn (40) for a determination of α_s. The result is in agreement with other measurements at similar Q^2, with remarkably competitive errors [77].

10. The spin structure of nucleons

The most straightforward interpretation of the violation of the Ellis – Jaffe sum rule is a non-zero polarisation of the strange sea. For a nucleon with spin $S_z = +1/2$, the moments Δq_i of parton distributions $q_i^+(x) - q_i^-(x)$ [cf. Eqn (34)] can be understood as normalised average z components of S_z carried by each of the quark flavours i, such that $\Delta\Sigma = \Delta u + \Delta d + \Delta s$ is the total quark contribution to S_z which can be decomposed according to the helicity sum rule

$$S_z = \frac{1}{2}\Delta\Sigma + \Delta G + L_z, \quad (41)$$

where L_z is the parton angular momentum. The Ellis – Jaffe prediction of Eqn (39) is equivalent to $\Delta\Sigma = \Delta u + \Delta d \approx 0.6$.

The formalism of Ellis and Jaffe relating moments of quark distributions to weak axial-vector couplings [33] therefore allows to analyse the measured moments of g_1 in terms of the flavour decomposition of the nucleon spin. All experiments have published results on $\Delta\Sigma$ and on the strange contribution Δs (Table 3); some care must be exercised in comparing these results since they refer to different Q^2 and were evaluated with different assumptions on the QCD radiative corrections. The same data are therefore shown in Fig. 16, where they are evaluated from the experimental moments with a consistent treatment of QCD corrections at a common $Q^2 = 5$ GeV^2. With the exception of E142, all data lead to the conclusion that the total quark contribution is small, $\Delta\Sigma \approx 0.2$, and that there is a small but significant negative contribution from the strange sea, $\Delta s \approx -0.1$.

The most reliable combined result is again obtained by combining the data at the level of g_1 and including the small-x behaviour observed in Fig. 12 into the calculation of Γ_1 for all deuteron and neutron data. Assuming that $\Delta\Sigma$ and Δs are the

Table 3. Experimental results on the total ($\Delta\Sigma$) and strange (Δs) quark contributions to the nucleon spin. The EMC result also includes earlier SLAC E80 and E130 data and is re-evaluated from Ref. [32] using up-to-date parametrisations of F_2 and R. For references see Table 2

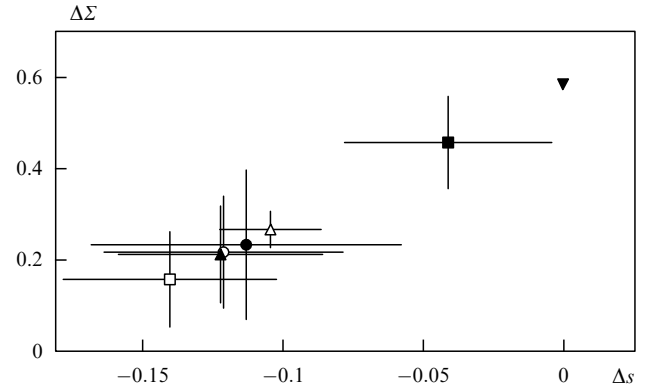| Experiment	Target	Q^2, GeV^2	$\Delta\Sigma$	Δs
EMC	p	10.7	0.27 ± 0.16	-0.10 ± 0.05
SMC	p	10	0.22 ± 0.14	-0.12 ± 0.06
	d	10	0.20 ± 0.11	-0.12 ± 0.04
E142	n	2	0.57 ± 0.11	-0.01 ± 0.06
E143	p	3	0.27 ± 0.10	-0.10 ± 0.04
	d	3	0.30 ± 0.06	-0.09 ± 0.02

Figure 16. Experimental results on the total ($\Delta\Sigma$) and strange (Δs) quark contributions to the nucleon spin at $Q^2 = 5$ GeV^2: ■ — E142 (neutron), □ — E143 (proton), △ — E143 (deuteron), ▲ — SMS (deuteron), ○ — SMS (proton), ● — EMC (proton), ▼ — the Ellis – Jaffe prediction.

same for proton, neutron, and deuteron, a fit with proper treatment of correlated errors, similar to the one discussed above, gives

$$\Delta\Sigma = 0.19 \pm 0.07, \quad \Delta s = -0.13 \pm 0.02$$

at $Q^2 = 5$ GeV^2. From a different analysis, based on a smaller data sample and a less detailed treatment of the experimental errors, Ellis and Karliner find

$$\Delta\Sigma = 0.31 \pm 0.07, \quad \Delta s = -0.10 \pm 0.03$$

at $Q^2 = 5$ GeV^2 [77]. It is worth remembering that these analyses rely on the assumption of exact flavour SU(3) symmetry to justify the use of measurements of F/D from hyperon decays. A recent study [82] has shown that $\Delta\Sigma$ is almost insensitive to SU(3)$_f$ breaking effects, whereas the absolute value of Δs can decrease substantially under reasonable assumptions on SU(3)$_f$ symmetry breaking.

The above analyses account for QCD radiative corrections, whereas the 'anomalous' contribution to the singlet coupling a_0 is usually ignored, again due to our lack of knowledge of ΔG.

A generalisation of the SMC analysis [83] discussed above which accounts for the axial anomaly is shown in Fig. 17. It illustrates that, from the present data, a gluon distribution with $\Delta G \approx 3$ is required to restore the Ellis – Jaffe sum rule.

11. Conclusions

Deep inelastic muon scattering experiments performed in collaboration with JINR and CERN have produced a wealth of significant results, many of which have passed the test of time already and are cornerstones of our present understanding of the dynamical structure of protons and neutrons. In particular, they have proven to be powerful tools to test predictions of QCD, such as scaling violations of structure functions and the Bjorken sum rule.
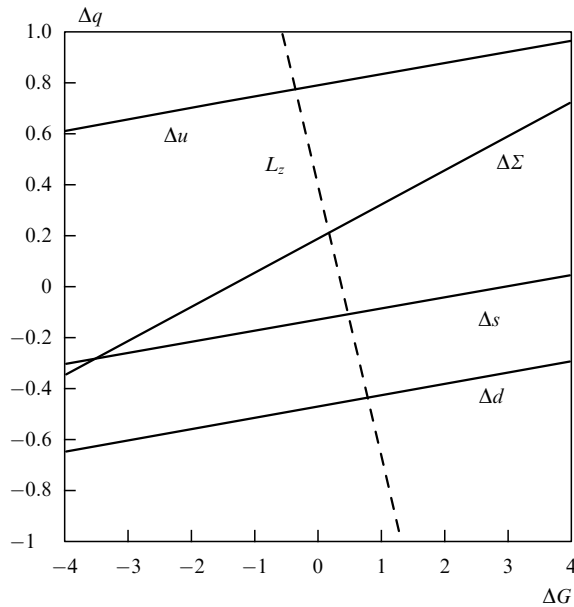
Figure 17. Quark contributions to the nucleon spin as a function of the first moment of the polarised gluon distribution, at $Q^2 = 5$ GeV^2. Also shown is the total quark angular momentum L_z required to fulfill the relation $S_z = 1/2 = (1/2)\Delta\Sigma + \Delta G + L_z$.

References

1. See, e. g., Riordan M *The Hunting of the Quark* (New York: Simon and Schuster, 1987); Taylor R, in *Proc. 19th SLAC Summer Institute on Particle Physics* (Ed. J Hawthorne) (SLAC-REPORT-398, 1991)
2. Feynman R P *Photon – Hadron Interactions* (Redwood City, Calif.: Addison Wesley Publ. Co., Advanced Book Program, 1989)
3. Close F E *An Introduction to Quarks and Partons* (London, New York: Academic Press, 1979)
4. Halzen F, Martin A D *Quarks and Leptons* (New York: John Wiley and Sons, 1984)
5. Roberts R G *Structure of the Proton: Deep Inelastic Scattering* (Cambridge: Cambridge University Press, 1990)
6. Eisele F *Rep. Prog. Phys.* **49** 233 (1986)
7. Diemoz M, Ferroni F, Longo E *Phys. Rep.* **130** 293 (1986)
8. Sloan T, Smadja G, Voss R *Phys. Rep.* **162** 45 (1988)
9. Mishra S R, Sciulli F, in *Annual Review of Nuclear and Particle Science* (Eds J D Jackson et al.) Vol. 39 (Palo Alto, CA, USA: Annual Review, 1989) p. 259
10. Virchaux M, in *Proc. Workshop "QCD, 20 years later"* (Eds P Zerwas, H A Kastrup) (Aachen, 1992)
11. For a recent review see Arneodo M, CERN-PPE/92-113 (1992) (subm. to *Phys. Rep.*)
12. Prescott C Y et al. *Phys. Lett. B* **77** 347 (1978); *Phys. Lett. B* **84** 524 (1979)
13. BCDMS: Argento A et al. *Phys. Lett. B* **120** 245 (1983); *Phys. Lett. B* **140** 142 (1984)
14. Callan C G, Gross D J *Phys. Rev. Lett.* **22** 156 (1969)
15. Altarelli G, Martinelli G *Phys. Lett. B* **76** 89 (1978)
16. EMC: Allkofer O C et al. *Nucl. Instrum. Methods* **179** 445 (1981); Albanese J P et al. *Nucl. Instrum. Methods Phys. Res.* **212** 111 (1983)
17. BCDMS: Bollini D et al. *Nucl. Instrum. Methods Phys. Res.* **204** 333 (1983); Benvenuti A C et al. *Nucl. Instrum. Methods Phys. Res.* **226** 330 (1984)
18. BCDMS: Benvenuti A C et al. *Phys. Lett. B* **195** 97 (1987)
19. BCDMS: Benvenuti A C et al. *Phys. Lett. B* **223** 485 (1989)
20. BCDMS: Benvenuti A C et al. *Phys. Lett. B* **237** 592 (1990)
21. Whitlow L W et al. *Phys. Lett. B* **282** 475 (1992)
22. Arneodo M et al. *Phys. Lett. B* **364** 107 (1995)
23. Adams M R et al., FNAL-PUB-95/396-E (1995) (subm. to *Phys. Rev. D*)
24. Altarelli G *Phys. Rep.* **81** 1 (1982)
25. Hansl T, in *Proc. 19th SLAC Summer Institute on Particle Physics* (Ed. J Hawthorne) (SLAC-REPORT-398, 1991)
26. Bardeen W A et al. *Phys. Rev. D* **18** 3998 (1978)
27. Altarelli G, Parisi G *Nucl. Phys. B* **126** 298 (1977)
28. BCDMS: Benvenuti A C et al. *Phys. Lett. B* **195** 97 (1987)
29. BCDMS: Benvenuti A C et al. *Phys. Lett. B* **223** 490 (1989)
30. Virchaux M, Milsztajn A *Phys. Lett. B* **274** 221 (1992)
31. Ellis R K, Furmanski W, Petronzio R *Nucl. Phys. B* **212** 29 (1983)
32. EMC: Ashman J et al. *Phys. Lett. B* **206** 364 (1988); *Nucl. Phys. B* **328** 1 (1989)
33. Ellis J, Jaffe R *Phys. Rev. D* **9** 1444 (1974); **10** 1669 (1974)
34. Reya E, in *Proc. XXXII Internationale Universitätswochen für Kern- und Teilchenphysik* (Austria, Schaldming, 1993) (Eds L Mathelitsch, W Plessas) (Springer-Verlag, 1994) p. 175
35. Forte S, in *Proc. Tennessee International Symposium on Radiative Corrections* (Tennessee, Gatlinburg, 1994) (hep-ph-9409416) †
36. Jaffe R L *Comm. Nucl. Part. Phys.* **19** 239 (1990)
37. Hoodbhoy P, Jaffe R L, Manohar A *Nucl. Phys. B* **312** 571 (1989); Rodriguez M A, PhD Thesis (University of Santiago di Compostela, 1994)
38. Doncel M G, de Rafael E *Nuovo Cimento* **4A** 363 (1971); Gnädig P, Niedermayer F *Nucl. Phys. B* **55** 612 (1973)
39. Ji X, in *Proc. Workshop on Deep Inelastic Scattering and QCD* (Eds J-F Laporte, Y Sirois) (Paris, 1995)
40. Wandzura S, Wilczek F *Phys. Lett. B* **72** 195 (1977)
41. Burkhardt H, Cottingham W N *Ann. Phys.* (*N.Y.*) **56** 453 (1970)
42. SMC Proposal: CERN/SPSC 88-47 (SPSC P242) (1988); CERN/SPSLC 94-13 (SPSC/P242/Add. 1) (1994); CERN/SPSLC 95-28 (SPSC/P242/Add. 2) (1995)
43. Arnold R et al., SLAC Proposal E-142 (1989); SLAC Proposal E143 (undated); SLAC Proposal E154 (1993); SLAC Proposal E155 (1993)
44. HERMES Proposal, DESY PRC 90/01 (1990); HERMES Technical Design Report (1993)
45. SMC: Adeva B et al., Preprint CERN-PPE/95-31 (1995) (subm. to *Phys. Rev. Lett.*)
46. SMC: Adeva B et al. *Nucl. Instrum. Methods* **343** 363 (1994)
47. EMC: Allkofer O C et al. *Nucl. Instrum. Methods* **179** 445 (1981)
48. Chupp T E et al. *Phys. Rev. C* **45** 915 (1992); *Phys. Rev. C* **36** 2244 (1987)
49. Crabb D G, Day D, in *Proc. 7th Workshop on Polarised Target Materials and Techniques* (Germany: Bad Honnef, 1994) (to be published in *Nucl. Instrum. Methods*)
50. SMC: Adeva B et al. *Phys. Lett. B* **302** 533 (1993)
51. SMC: Adams D et al. *Phys. Lett. B* **329** 399 (1994) [erratum: *Phys. Lett. B* **339** 332 (1994)]
52. SMC: Adams D et al. *Phys. Lett. B* **336** 125 (1994)
53. SMC: Adams D et al., Preprint CERN-PPE/95-97 (subm. to *Phys. Lett. B*)
54. Magnon A, in *Proc. Workshop on Deep Inelastic Scattering and QCD* (Eds J-F Laporte, Y Sirois) (Paris, 1995)
55. E142: Anthony P L et al. *Phys. Rev. Lett.* **71** 959 (1993)
56. E143: Abe K et al. *Phys. Rev. Lett.* **74** 346 (1995)
57. E143: Abe K et al., SLAC-PUB-95-6734 (1995)
58. Roblin Y, in *Proc. Workshop on Deep Inelastic Scattering and QCD* (Eds J-F Laporte, Y Sirois) (Paris, 1995)
59. Altarelli G, Stirling W J *Particle World* **1** 40 (1989); Altarelli G, Nason P, Ridolfi G *Phys. Lett. B* **320** 152 (1994) [erratum: *Phys. Lett. B* **325** 538 (1994)]
60. Altarelli G, Ross G G *Phys. Lett. B* **212** 391 (1988)
61. Ball R D, Forte S, Ridolfi G, CERN-TH/95-31 (GeF-TH-2/95) (hep-ph-9502340)
62. Gehrmann T, Stirling W J *Z. Phys. C* **65** 461 (1995)
63. NMC: Amaudruz P et al. *Phys. Lett. B* **295** 159 (1992)
64. Whitlow L W et al. *Phys. Lett. B* **250** 193 (1990); Whitlow L W, PhD Thesis, SLAC-Report-357 (Stanford University, 1990)
65. Buck W W, Gross F *Phys. Rev. D* **20** 2361 (1979); Zuilhof M J, Tjon J A *Phys. Rev. C* **22** 2369 (1980); Lacombe M et al. *Phys. Rev. C* **21** 861 (1980); Machleidt R, Holinde K, Elster Ch *Phys. Rep.* **149** 1

† See, for example, http: //xxx.lanl.gov/archive/.

(1987); Umnikov A Yu et al., University of Alberta Preprint Alberta-Thy-29-94 (1994)

66. E130: Baum G et al. *Phys. Rev. Lett.* **51** 1135 (1983)

67. E143: Grenier Ph, in *Proc. XXIXth Rencontres de Moriond* (Les Arcs, Savoie, France, 1995) (in print)

68. Heimann R L *Nucl. Phys. B* **64** 429 (1973); Ellis J, Karliner M *Phys. Lett. B* **213** 73 (1988)

69. Schäfer A *Phys. Lett. B* **208** 175 (1988)

70. Bass S D, Landshoff P V *Phys. Lett. B* **336** 537 (1994)

71. Close F E, Roberts R G *Phys. Lett. B* **336** 257 (1994) (and references therein)

72. Ahmed M A, Ross G G *Phys. Lett. B* **56** 385 (1975)

73. Particle Data Group: Montanet L et al. *Phys. Rev. D* **50** 1173 (1994)

74. Close F E, Roberts R G *Phys. Lett. B* **316** 165 (1993)

75. Larin S A, Tkachev F V, Vermaseren J A M *Phys. Rev. Lett.* **66** 862 (1991); Larin S A, Vermaseren J A M *Phys. Lett. B* **259** 345 (1991); Larin S A, CERN-TH-7208/94 (hep-ph-9403383)

76. Larin S A *Phys. Lett.* **334** 192 (1994)

77. Ellis J, Karliner M *Phys. Lett. B* **341** 397 (1995)

78. Bjorken J D *Phys. Rev.* **148** 1467 (1966); *Phys. Rev. D* **1** 1376 (1970)

79. Kodaira J et al. *Phys. Rev. D* **20** 627 (1979); Kodaira J et al. *Nucl. Phys. B* **159** 99 (1979)

80. Kodaira J *Nucl. Phys. B* **165** 129 (1980)

81. See, e.g., Voss R, in *Proc. XVI Int. Symposium on Lepton – Photon Interactions, Cornell University, Ithaca, New York, 1993* (Eds P Drell, D Rubin) (New York: AIP Press, 1994) p. 144

82. Lichtenstadt J, Lipkin H J, TAUP-2244-95 (WIS-95/15/Mar-PH) (hep-ph-9504277)

83. Stiegler U, in *Proc. IVth Int. Symposium on Weak and Electromagnetic Interactions in Nuclei* (Osaka, 1995) (in print)

84. Perrot-Kunne F, in *Proc. Workshop on Deep Inelastic Scattering and QCD* (Eds J-F Laporte, Y Sirois) (Paris, 1995)